

## Investigation of laser-induced plasma in SF<sub>6</sub> at different pressures using Thomson scattering

Cite as: Phys. Plasmas **27**, 073508 (2020); <https://doi.org/10.1063/5.0009906>

Submitted: 07 April 2020 . Accepted: 26 June 2020 . Published Online: 10 July 2020

Hao Sun, Haodong Chang, Mingzhe Rong, Yi Wu , and Hantian Zhang 



[View Online](#)



[Export Citation](#)



[CrossMark](#)

### ARTICLES YOU MAY BE INTERESTED IN

**Transition from snowplow to deflagration mode in a gas-prefilled parallel-plate plasma accelerator**

Physics of Plasmas **27**, 073509 (2020); <https://doi.org/10.1063/5.0008998>



# Investigation of laser-induced plasma in SF<sub>6</sub> at different pressures using Thomson scattering

Cite as: Phys. Plasmas **27**, 073508 (2020); doi: 10.1063/5.0009906

Submitted: 7 April 2020 · Accepted: 26 June 2020 ·

Published Online: 10 July 2020



View Online



Export Citation



CrossMark

Hao Sun, Haodong Chang, Mingzhe Rong,<sup>a)</sup> Yi Wu, and Hantian Zhang<sup>a)</sup>

## AFFILIATIONS

State Key Laboratory of Electrical Insulation and Power Equipment, Xi'an Jiaotong University, Xi'an, Shaanxi 710049, People's Republic of China

<sup>a)</sup>Authors to whom correspondence should be addressed: mzrong@xjtu.edu.cn and saphirezhang@gmail.com

## ABSTRACT

Thomson scattering was applied to measure the electron density and temperature in laser-induced SF<sub>6</sub> plasmas at various pressures (0.2–2 atm). The plasma was induced by the Nd:YAG laser (1064 nm, 200 mJ, and 7 ns) focused into a chamber filled with SF<sub>6</sub>. A second harmonic Nd:YAG laser (532 nm, 50 mJ, and 6 ns) was used to probe the distributions of electron density and temperature. The images after breakdown indicate that higher pressure accelerates the plasma evolution and enhances the asymmetry of the plasma structure. Additionally, different from toroidal structures in other gases, a special vortex structure appeared in SF<sub>6</sub>. The electron density around the axis at 0.2 atm decreases from  $1.66 \times 10^{23} \text{ m}^{-3}$  at 2  $\mu\text{s}$  to  $4.50 \times 10^{22} \text{ m}^{-3}$  at 6  $\mu\text{s}$ , and meanwhile, the electron temperature drops from 22 050 K to 15 600 K. At 2 atm, from 2  $\mu\text{s}$  to 6  $\mu\text{s}$ , the electron density decreases from  $3.00 \times 10^{23} \text{ m}^{-3}$  to  $5.23 \times 10^{22} \text{ m}^{-3}$  and the temperature drops from 44 000 K to 14 800 K. The time exponent obtained by fitting the maximum electron density using the power law decreases from -1.206 to -1.669 in the pressure range from 0.2 atm to 2 atm, indicating that the pressure increases the decaying rate of electron density. From 0.4 atm to 2 atm, the time exponent of the decay of electron temperature decreases from -0.499 to -0.926. The comparisons among laser-induced plasmas in various gases show that the decaying rates of both electron density and temperature in SF<sub>6</sub> are superior to air and argon.

Published under license by AIP Publishing. <https://doi.org/10.1063/5.0009906>

## I. INTRODUCTION

Laser-induced plasma (LIP) is of great importance in many applications including the laser-triggered gas switch (LTGS),<sup>1</sup> laser propulsion,<sup>2</sup> and laser-induced breakdown spectroscopy (LIBS).<sup>3</sup> In pulsed power systems, the gas switch filled with high-pressure SF<sub>6</sub> has been used to provide the low jitter and high current capacity.<sup>4,5</sup> SF<sub>6</sub> is also widely used in power equipment, like gas insulated switchgear (GIS) and gas insulated transmission line (GIL), due to its superior arc quenching ability and insulation performance. Also, in the semiconductor industry, low-pressure SF<sub>6</sub> is chosen as the working gas to improve the etching process.<sup>6</sup>

The electron density and temperature are important to understand the generation, evolution, and decay of laser-induced plasmas. For example, the coefficient of inverse bremsstrahlung radiation, one of the major absorption mechanisms of laser energy, is closely related to the electron temperature and density.<sup>7</sup> The measurement of electron parameters is also important to reduce the uncertainty of the measurement of laser-induced breakdown spectroscopy (LIBS).<sup>8</sup>

Research on the characterization of LIPs has been reviewed recently.<sup>9,10</sup> Optical emission spectroscopy (OES) is generally used due

to its simple experimental setup and non-intrusive characteristic.<sup>11,12</sup> However, much effort must be made to interpret the spectral data since the technique depends on many assumptions; for example, the plasma should be assumed to be symmetric or optically thin. An alternative diagnostic method to OES is laser Thomson scattering. It has the advantage of high spatial-temporal resolution. The electron density and temperature can be simultaneously obtained by fitting the electron features of the scattered spectrum. Moreover, this measurement does not rely on the local thermodynamic equilibrium (LTE) assumption. The development of pulsed laser sources and intensified CCD (ICCD) have made the laser Thomson scattering a powerful tool to investigate LIP over the past two decades. Zhang *et al.*<sup>13</sup> and Dzierżęga *et al.*<sup>14</sup> measured the electron density and temperature of LIP in air. The heating effect introduced by the probe laser on the plasma was studied by adjusting the delay between the probe laser and ICCD.<sup>15</sup> LIPs in helium or helium-nitrogen mixtures and argon were investigated by Nedanovska *et al.*<sup>16</sup> and Mendys *et al.*,<sup>17</sup> respectively. However, the related study on SF<sub>6</sub> plasma is yet absent.

The purpose of this work is to present a spatially and temporally resolved measurement of LIPs in SF<sub>6</sub> at various pressures by Thomson

scattering. The decays of electron temperature and electron number density were compared with those in air and argon. The influence of pressures on the electron parameters was also discussed.

## II. EXPERIMENTAL SETUP AND METHODS

Figure 1 illustrates the experimental setup. Two Nd:YAG lasers operating at 5 Hz were used as the breakdown laser (to generate the plasma) and probe laser (to generate the scattering signal), respectively. The breakdown laser (Beamtech, Nimma-900; wavelength, 1064 nm; pulse width, 7 ns) was focused by a plano-convex lens with a focal length of 100 mm. Its energy was 200 mJ, and the radius at  $1/e^2$  was about 90  $\mu\text{m}$ . Hence, the fluence of the breakdown laser (gaussian beam) was about 1.5  $\text{kJ}/\text{cm}^2$ , resulting in a highly reproducible plasma. The probe laser (Litron, Nano L 200-15, 532 nm, 6 ns, 50 mJ) was set perpendicular to the breakdown laser and focused using another plano-convex lens ( $f=300 \text{ mm}$ ), and at the focus, the minimum spot size was 500  $\mu\text{m}$ , while the laser fluence was 20  $\text{J}/\text{cm}^2$ . For the probe laser, an attenuator composed of a half-wave plate and a Glan-Thompson polarizer was used to adjust the energy and to provide a specified polarization state. The two lasers propagated through the windows on the chamber and were focused around the center of the chamber. The chamber was pumped to a pressure level less than 5 Pa and then filled with 99.999% SF<sub>6</sub> to a certain pressure. This process was repeated three times to reduce the gas impurity.

The images of the plasma were recorded using an ICCD in the  $y$  direction. The scattered light was also collected in the same direction. It should be noted that they were not recorded simultaneously. A radially resolved signal can be obtained by rotating the image of the plasma onto the entrance slit of the spectrometer. A wavelength range from 522.4 nm to 541.6 nm was used to record the spectral signal. The triggers of both lasers and ICCD were accurately controlled using a digital delay generator (Stanford Research, DG535). More details about the experimental setup can be found in our previous work.<sup>13</sup>

Thomson scattering<sup>18</sup> is the interaction between low-energy photons and electrons in the plasma. The density fluctuation of free

electrons in the electric field of the laser forms the “electron feature,” which is a featured scattering spectrum symmetrically located around the wavelength of the incident laser. This interaction can be either in the collective or non-collective regime according to the scattering parameter  $\alpha$  as follows:

$$\alpha = \frac{\lambda_0}{4\pi \sin(\theta/2)} \sqrt{\frac{4\pi n_e e^2}{\epsilon_0 k_B T_e}}, \quad (1)$$

where  $\theta$  is the scattering angle,  $\lambda_0$  is the wavelength of the probe laser,  $n_e$  is the electron density/ $\text{m}^{-3}$ ,  $T_e$  is the electron temperature,  $k_B$  is the Boltzmann constant,  $e$  is the charge of an electron, and  $\epsilon_0$  is the permittivity in vacuum. When  $\alpha \ll 1$  (non-collective), an absolute calibration of the detecting system is necessary, and the scattering signal can be fitted with a Gaussian profile. In the collective regime, the scattering parameter is over 1, and the electron feature shows two sidebands, which are symmetric about the wavelength of the probe laser. Therefore, the scattered spectrum can be simulated following the Salpeter approximation.<sup>19</sup>

$$S(k, \omega) = \frac{C}{|1 + \alpha^2 W(\xi)|^2} \frac{e^{-\xi^2}}{k v_{te}}, \quad (2)$$

where  $\xi_j = \frac{\omega}{kv_{te}}$ ,  $\omega = \omega_s - \omega_i$  is the frequency difference between scattering light and the probe laser,  $k = |k| = \frac{4\pi}{\lambda_0} \sin\left(\frac{\theta}{2}\right)$ ,  $v_{te} = \sqrt{\frac{2k_B T_e}{m_e}}$ ,  $m_e$  is the mass of electron, and  $W(\xi) = 1 - 2\xi e^{-\xi^2} \int_0^\xi e^{\zeta^2} d\zeta + i\sqrt{\pi} \xi e^{-\xi^2}$ . In this work, the scattering signals were mainly in the collective regime ( $\alpha$  ranged from 3 to 20), which can be derived from the results shown in later sections. According to the suggestion by Kelly and Gary,<sup>20</sup>  $1 \leq \alpha \leq 1.5$  is a transition region between the collective regime and non-collective regime. Therefore, the Salpeter approximation should be valid and applied for data processing. The electron density and temperature were derived by fitting the measured electron features with the calculated profile. More information about the theory

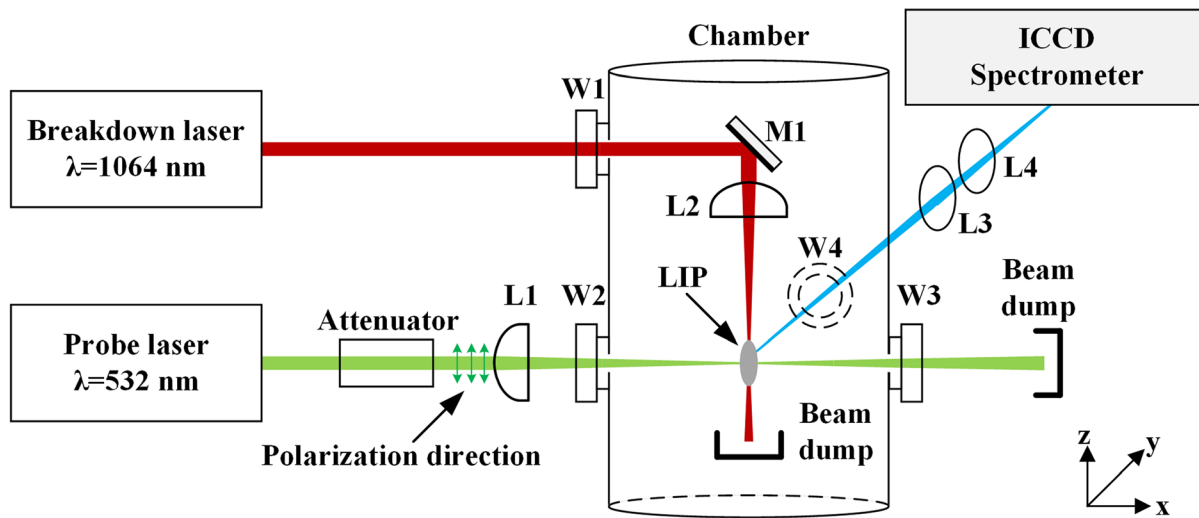


FIG. 1. Schematic view of the experimental setup. L1 and L2—plano-convex lenses, L3 and L4—achromatic lenses, W1, W2, W3, and W4—windows, and M1—mirror.

of Thomson scattering and data interpretation can be found in Refs. 21 and 22.

It is important for the laser Thomson scattering to achieve an adequate signal-to-noise ratio without introducing too much perturbation to the plasma. It is known that although the probe does not considerably affect  $n_e$ , it can lead to the overestimation of  $T_e$ .<sup>15</sup> According to the theoretical calculation and experimental investigation of LIPs in argon,<sup>17</sup> the increase in  $T_e$  was negligible when the probe laser with a fluence lower than  $20 \text{ J/cm}^2$  was applied. Another research about the heating effect of the probe laser in air LIP<sup>15</sup> showed that the overestimation of  $T_e$  was considerable (30%) during the very beginning of the breakdown (<500 ns), while the overestimation nearly vanished after 600 ns. Therefore, the fluence of the probe laser was carefully tuned to around  $20 \text{ J/cm}^2$  to avoid significant heating effects.

### III. RESULTS AND DISCUSSION

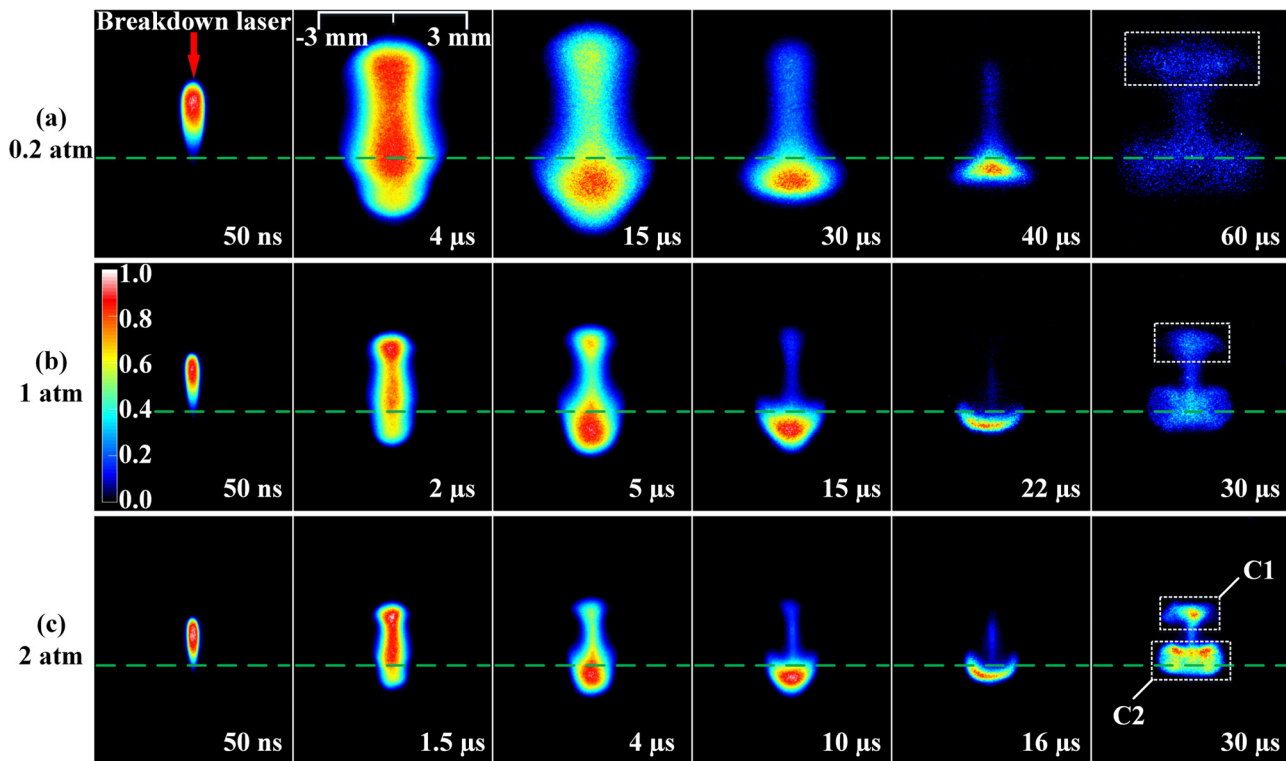
#### A. Evolution of self-emission images

Figure 2 shows the temporal evolution of laser-induced plasmas at three different pressures. The images at 50 ns were just integrated by 10 shots, when the optical emission of LIP is quite strong. With the decay of the plasma, each image was obtained by integrating 100 shots. The gate width of the ICCD varied from 2 ns to 100 ns depending on the different stages of the decay. The green dashed lines indicate the path of the probe laser and the position where the plasmas were initially ignited.

At 0.2 atm, the contours of plasma maintain a good symmetry about the axis. However, the symmetry of plasma is disturbed at higher pressure, for example, the plasma at 4  $\mu\text{s}$  and 2 atm. The asymmetric distribution was attributed to the non-uniform deposition of the energy of the breakdown laser.<sup>23</sup> Such a phenomenon was also reported by Sasoh *et al.*<sup>24</sup>

At 50 ns, plasmas at all pressures expand toward the incident direction of the breakdown laser and tend to move away from the initial breakdown point. The reason for this movement is that the gas around the focus is excited by strong laser energy, and soon, it is no longer optically thin. Then, the plasma on the side toward the incident breakdown laser absorbs more energy and thus develops faster than the other side. The plasma is initially in the shape of teardrop, and its size decreases with pressure, which is consistent with the observation by Nassif and Hüwel.<sup>25</sup> After the formation of the teardrop shape, the plasma continues to expand radially. In the axial direction, the plasma emission is stronger in the lower region, as shown in the third images at each pressure of Fig. 2. In this stage, the bremsstrahlung process is the main mechanism for the fast decay of plasma. After that, at 15  $\mu\text{s}$  and 1 atm, for example, the top half of plasma shrinks sharply, making the shape of plasma an inverted “umbrella,” which is even more obvious at 22  $\mu\text{s}$  at 1 atm.

During the late period, two independent expansion regions (marked by C1 and C2 in Fig. 2) appear along the axis. The maximum emission of C2 is comparable with that of C1, and the former is always larger than the latter in size. Two off-axis regions with strong emission



**FIG. 2.** Temporal evolutions of the emission from  $\text{SF}_6$  plasma at three pressures: (a) 0.2 atm, (b) 1 atm, and (c) 2 atm. All images are normalized to their maximum intensity. The breakdown laser is incident from top to bottom along the center of each image, while the probe laser propagates along the direction marked by the green dashed line.

can also be seen in C2 at 30  $\mu\text{s}$  and 2 atm, which indicates a toroidal structure in the lower half of the plasmas. The moment for the formation of the toroidal structure depends on the pressure. The higher pressure would make the toroidal structure appear sooner. For example, it takes about 50  $\mu\text{s}$  to form the toroidal structure at 0.2 atm, while it takes only 20  $\mu\text{s}$  at 2 atm. Ghosh and Mahesh<sup>26</sup> simulated the fluid field and temperature evolution in air LIP. The appearance of the toroidal structure is due to the injection of high-speed cold gas into C1 (in the direction opposite to the breakdown laser) and the subsequent generation of complex vortices. A similar structure was also reported in argon.<sup>17</sup> However, the transformation into the torus in the air plasma (using the same experimental setup<sup>13</sup>) takes shorter time under the same conditions (laser energy and pressure). It seems that the transformation time is related not only to the pressure but also to the mass of the particles. Higher pressure or smaller molecules may reduce the transformation time. Nedanovska *et al.*<sup>23</sup> compared the transformation time of the laser spark in helium (10  $\mu\text{s}$ ) with those in argon (20–40  $\mu\text{s}$ ) and nitrogen (100  $\mu\text{s}$ ), and a similar conclusion that smaller molecules reduce the transformation time was obtained.

The special structure in C1 of Fig. 2 appears together with the toroidal structure. Bradley *et al.*<sup>27</sup> studied the laser-induced spark ignition of flammable, gaseous premixtures, and they found that the interaction of the rarefaction wave with the hot gas created this kind of pattern. They explained that during the late stage, as the rarefaction wave propagated outward, the hot gases near both C1 and C2 were accelerated inward, and thus, two toroidal structures appeared. Nevertheless, the toroidal structure in C1 disappears quickly because the gas here is accelerated to a higher velocity. Ghosh and Mahesh<sup>26</sup> made a detailed simulation of the laser-induced plasma in air. In the simulation of fluid dynamics, two vortex regions appeared along the axis, but in the experiment, only one toroidal vortex ring could be observed. The toroidal structure in their experiment was similar to the results in Fig. 2. Joarder *et al.*<sup>28</sup> studied the laser-induced plasma in air using schlieren imaging, and they combined the experimental results with their numerical modeling. They summarized that the toroidal

structure is caused by the roll up motions of the central region. They also pointed out that due to the initial energy deposition and physico-chemical properties of the medium, the flow field in vortices was not identical, and thus, the toroidal structures may be different. Due to the different thermodynamic and transport properties of SF<sub>6</sub>, two toroidal structures can be captured.

Figure 3 shows the temporal evolution of the maximum self-emission intensity varying with pressure. The maximum intensity at 6  $\mu\text{s}$  and 1 atm (gate width: 10 ns, accumulated times: 100, and gain level: 1000) was defined as 1. The maximum self-emission intensity of each point in Fig. 3 was used to normalize the corresponding data in Fig. 2. At all pressures, the intensity decreases monotonically with time except for the last point at 1 atm. The slight increase in the intensity at 1 atm may be caused by the noise of instruments since during the late period, the signal was extremely weak and the gain level of ICCD was large. The initial intensity increases with pressure, but finally, the result at 0.2 atm is the highest. This indicates that the high pressure increases the decaying rate.

## B. Evolution of electron density and temperature

Images of the Thomson scattering spectra are shown in Fig. 4. The horizontal axis is the wavelength, and the vertical axis is the radial direction of plasmas. The consecutive images were recorded by adjusting time delays between the breakdown laser and the probe laser. To improve the signal-to-noise ratio, the gate width of ICCD was adjusted to 15 ns to cover the pulse of the probe laser. Before 2  $\mu\text{s}$ , 10 shots were accumulated to obtain the images. From 2.5  $\mu\text{s}$  to 3.5  $\mu\text{s}$ , the number of shots increased to 25, while after that the number of shots was even set as 100. The white region at 532 nm, indicating that the signal was saturated, was a combination of both the Rayleigh scattering and Thomson scattering. This region can be well distinguished from the Thomson scattering signal of all cases in this work, and it was excluded during the fitting process. There are two absent regions (dark areas) at about 531.8 nm and 534.4 nm from 800 ns to 1500 ns, corresponding to the emission lines of S II, and they were created by

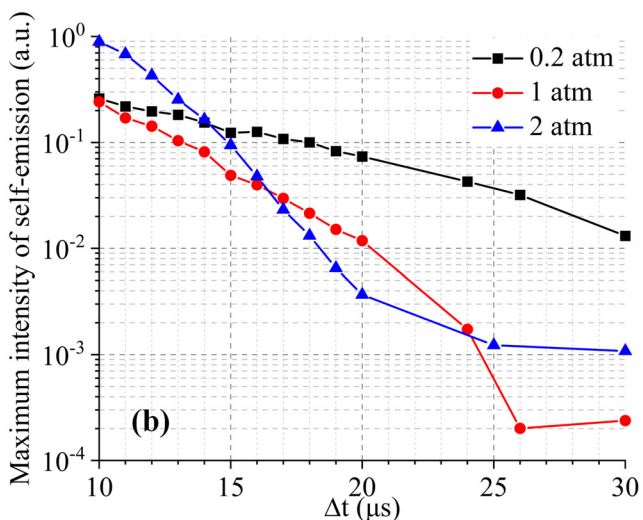
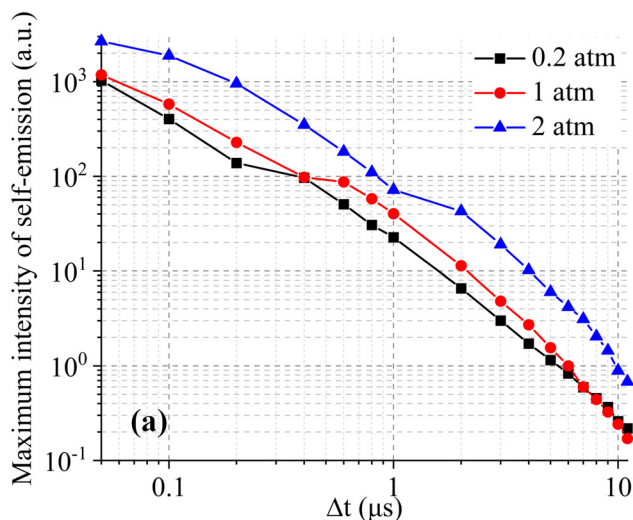
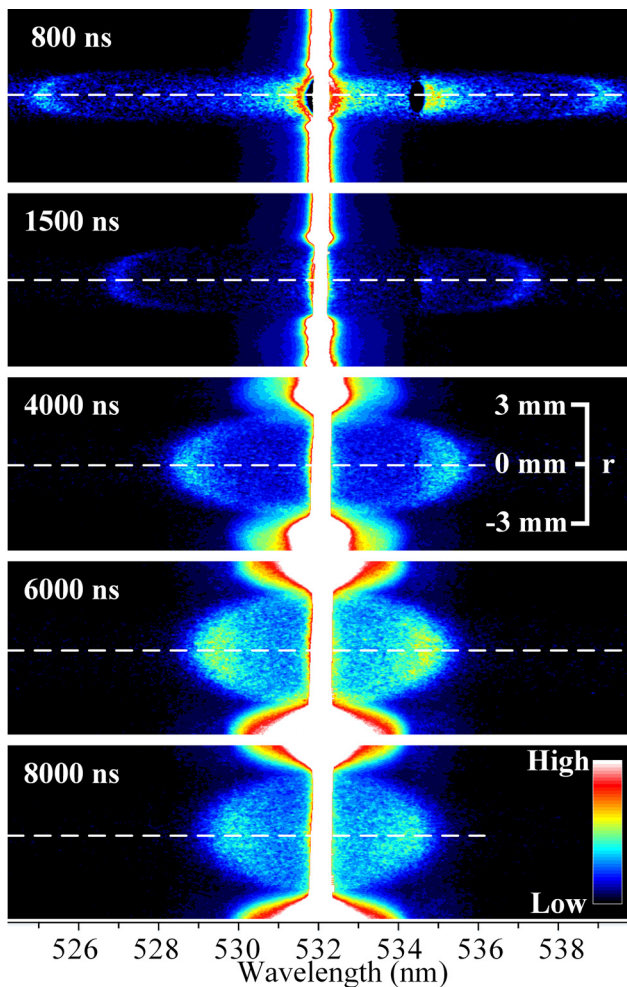


FIG. 3. Temporal evolution of the maximum self-emission intensity at different pressures: (a) 0.05–10  $\mu\text{s}$  and (b) 10–30  $\mu\text{s}$ .



**FIG. 4.** Thomson scattering spectra from 800 ns to 8000 ns at 0.2 atm. Each image is individually normalized to its maximum.

subtracting the self-emission spectra from the original scattering spectra. During the early stage, the emission lines are far from the two scattering sidebands, and a good fitting curve (Fig. 5) can be obtained. During the late stage, the intensity of the emission lines rapidly decreased, and good fitting curves can also be obtained. Therefore, the emission lines of S II had limited effects on the data fitting and were simply removed from the scattering spectra in this work. Raman scattering is the inelastic scattering of a photon by molecules, resulting in a change in the rotational and/or vibrational state of the molecules. Although the Raman spectrum was recorded in the research related to the laser-ablated metal plume,<sup>29,30</sup> it was weak and can be hardly seen in this work.

The electron feature of Thomson scattering appears as the two symmetric sidebands about the central wavelength of the probe laser. For time delays within 800 ns, although the electron temperature and density are considerably high, the plasma emission is strong, making the detection lose a reasonable signal-to-noise ratio. At 800 ns, the sidebands shift far from the central wavelength because of the

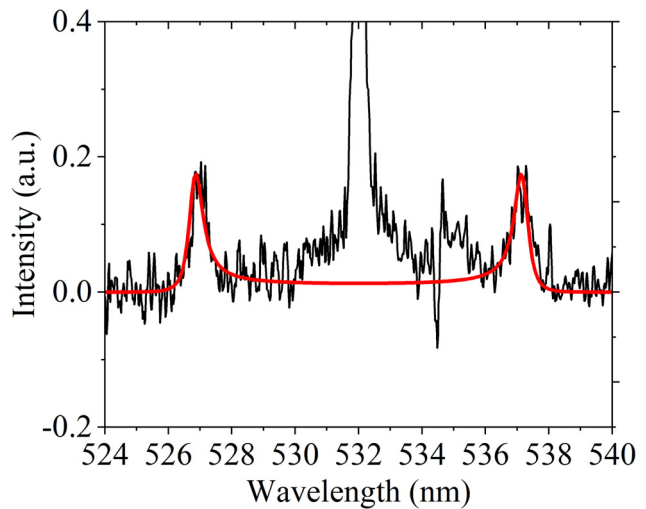


**FIG. 5.** Typical spectrum of the laser scattered signal (black curve) recorded at 1500 ns on the plasma axis. The fit curve (red curve) indicates that  $n_e = 2.3 \times 10^{23} \text{ m}^{-3}$  and  $T_e = 26\,500 \text{ K}$ .

extremely high electron temperature and density. The sidebands gradually become wider in the radial direction, and the values of their wavelength approach 532 nm. This means that the plasma expands radially, and simultaneously, the electron density and temperature keep decreasing. A good symmetry about the position of  $r = 0 \text{ mm}$  and a sharp gradient in the radius at the early stage are indicated by the two radial distributions of electron features, which can be observed during the whole process.

A typical spectrum of the laser scattered signal is shown in Fig. 5. During the data processing, the central part of the spectrum, including the plasma emission, Rayleigh scattering, the ion feature of Thomson scattering, and stray light, was excluded, and the range of wavelengths on the right half (532–540 nm) was carefully selected to reduce the interference of the emission line of S II. The electron density and temperature were then derived by fitting the theoretical function [Eq. (2)] to the experimental spectra. Two scattering sidebands can be separately fitted, making it feasible to obtain two sets of results of the electron temperature and density from each sideband. A careful comparison of fitting results between the left sideband in Fig. 5 ( $n_e = 2.24 \times 10^{23} \text{ m}^{-3}$  and  $T_e = 26\,000 \text{ K}$ ) and the right sideband ( $n_e = 2.32 \times 10^{23} \text{ m}^{-3}$  and  $T_e = 28\,000 \text{ K}$ ) also showed that the emission lines had little effect on the fitting results.

Figure 6 shows the radial distribution of the electron density  $n_e$  at different time delays  $\Delta t$  and pressures. The maximum electron density always exists around the axis of the plasma. At 2  $\mu\text{s}$ , good symmetrical distributions maintain at all pressures. As the pressure increases from 0.2 atm to 0.6 atm, the peak electron density increases from about  $1.6 \times 10^{23} \text{ m}^{-3}$  to  $2.6 \times 10^{23} \text{ m}^{-3}$ , and the radial gradient of electron density also increases. However, the maximum value of electron density tends to saturate when the pressure is increased further; for example, the peak values of both are around  $3.2 \times 10^{23} \text{ m}^{-3}$  at 1 atm and 2 atm. Besides, the measurable region shrinks with the increase in pressure due to the smaller size of the plasma at higher pressures (already shown in Fig. 2).

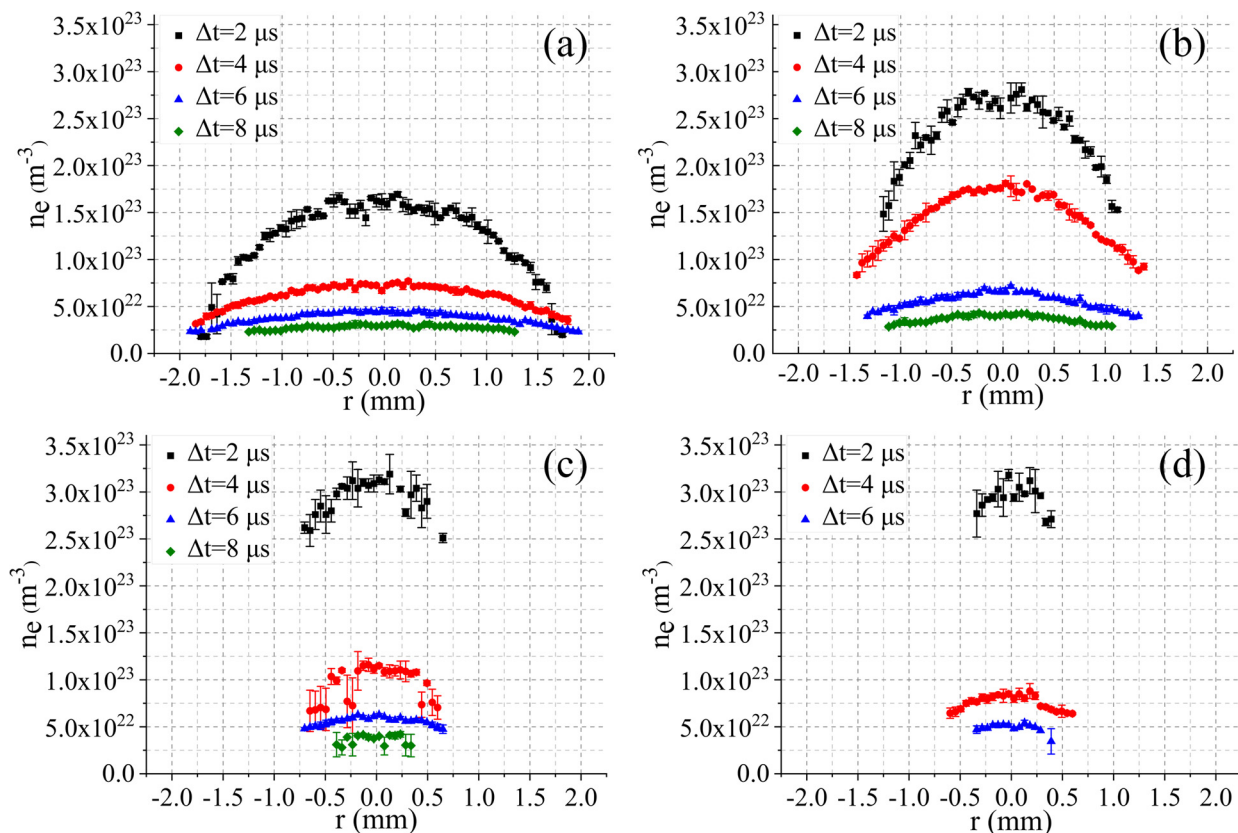


**FIG. 6.** Radial distribution of the electron density  $n_e$  at different time delays  $\Delta t$  and at four pressures: (a) 0.2 atm, (b) 0.6 atm, (c) 1 atm, and (d) 2 atm.

Subsequently, the distribution of electron density remains symmetrical, and its radial gradient becomes low at the pressure below 1 atm. For the pressures of 1 atm and 2 atm, the gradients are lower compared to those at 2  $\mu s$ , and the asymmetric distribution can be hardly seen after 4  $\mu s$ . The values of electron density in the radial direction at all pressures decrease with time. From 2  $\mu s$  to 4  $\mu s$ , the maximum electron density decreases by about 74% (from  $3.1 \times 10^{23} \text{ m}^{-3}$  to  $8.1 \times 10^{22} \text{ m}^{-3}$ ) at 2 atm, while a much slower decrease can be observed at 0.2 atm (from  $1.6 \times 10^{23} \text{ m}^{-3}$  to  $7.3 \times 10^{22} \text{ m}^{-3}$ ). Generally, the decaying rate of electron density increases with pressure.

The radial distribution of the electron temperature  $T_e$  at different time delays  $\Delta t$  and pressures is shown in Fig. 7. Different from the high gradient of the electron density in the radial direction at 2  $\mu s$  and 4  $\mu s$ , the temperature does not change significantly in radial directions<sup>31</sup> except for the data at 2 atm. It should be noted that the high gradient during the early stage may lead to an overestimation of electron temperature. Murphy<sup>32</sup> studied the plasmas of free-burning arcs and plasma jets, and the calculated electron temperature was found to be higher than the actual value in the focal range of the probe. At 2  $\mu s$ , the maximum temperature increases with pressure, i.e., from 26,200 K at 0.2 atm to 46,000 K at 2 atm. Two microseconds later, temperatures gradually decrease, and the temperatures around central regions are

within the range between 20,000 K and 25,000 K. From 2  $\mu s$  to 4  $\mu s$ , the peak temperature at 2 atm decreases most rapidly from 45,000 K to 25,000 K, which is almost twice the speed as the case at 1 atm. Afterward, no obvious difference in electron temperatures at various pressures can be inspected.

The temporal evolutions of  $n_e$  and  $T_e$  around the center (from  $r = -0.078 \text{ mm}$  to  $r = 0.078 \text{ mm}$  in Figs. 6 and 7) at different pressures are illustrated in Fig. 8. It is worth noting that the measurable time range is wider at lower pressure due to the weaker plasma emission and lower decaying rate. The electron density at 0.2 atm decreases from  $4.85 \times 10^{23} \text{ m}^{-3}$  at 0.8  $\mu s$  to  $1.83 \times 10^{22} \text{ m}^{-3}$  at 11  $\mu s$ . In the meantime, the measured electron temperature decreases from 40,000 K to 12,100 K. Increasing the pressure from 0.4 atm to 1 atm, the electron density at 2  $\mu s$  increases continually and finally reaches  $3.15 \times 10^{23} \text{ m}^{-3}$ , nearly twice as the result at 0.2 atm ( $1.67 \times 10^{23} \text{ m}^{-3}$ ). A similar trend can be found in the results of electron temperature.

The time-dependent decays of  $n_e$  and  $T_e$  were fitted with power laws  $A \cdot \Delta t^B$ ,<sup>22,30,33</sup> and the fitting parameters of electron density are listed in Table I. The value of the exponent  $B$ , which indicates the decaying rate, decreases as the pressure increases from 0.2 atm to 2 atm. This means that the decaying rate of  $n_e$  increases with pressure. After the breakdown, the induced plasma inside the focal region is rapidly excited by laser energy through the ionization processes, including

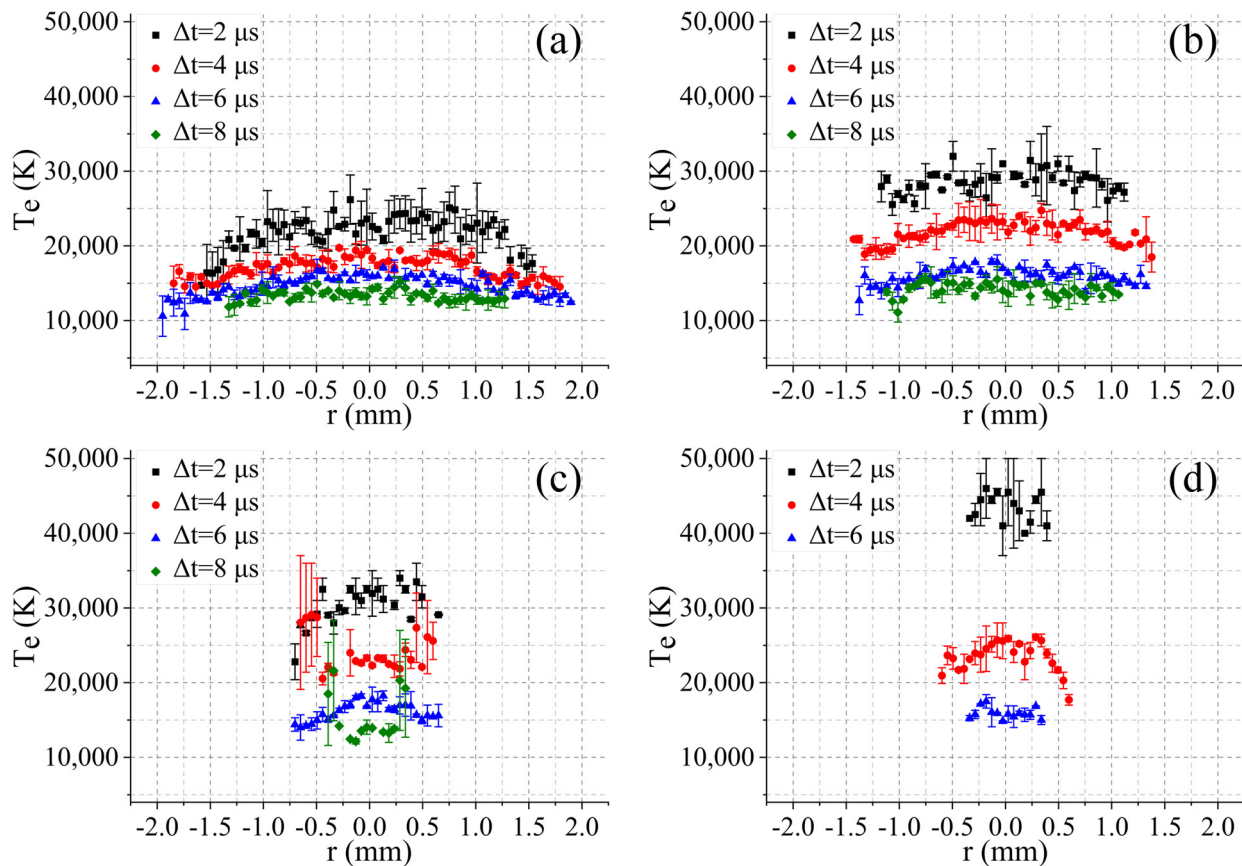


FIG. 7. Radial distribution of the electron temperature  $T_e$  at different time delays  $\Delta t$  and at four pressures: (a) 0.2 atm, (b) 0.6 atm, (c) 1 atm, and (d) 2 atm.

multiphoton ionization and cascade ionization. More electrons can be produced by the cascade ionization at higher pressure,<sup>27</sup> and then, the inverse bremsstrahlung process will be further enhanced since the coefficient of inverse bremsstrahlung is proportional to  $n_e^2$ .<sup>14</sup>

Therefore, plasma could absorb more energy per unit volume, increasing both the electron density and temperature at higher pressure. Glumac and Elliott<sup>34</sup> investigated the effect of ambient pressure on electron density in laser-induced air plasmas, and they summarized

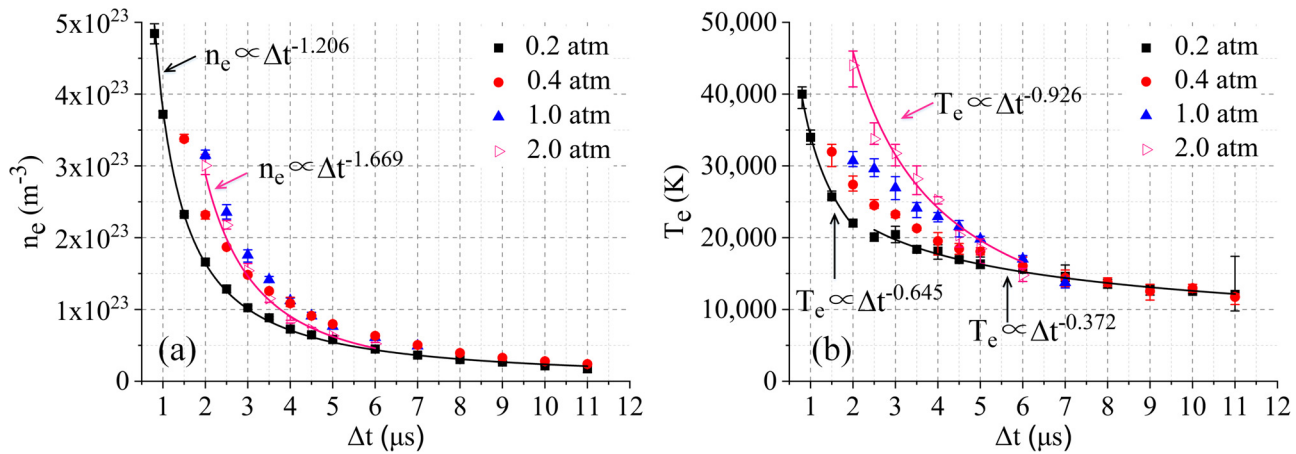


FIG. 8. Temporal evolution of the electron density (a) and temperature (b) around the center in the radial direction at various pressures.

**TABLE I.** Time exponents  $B$  of the decaying of electron density and temperature (0.2 atm–2.0 atm).

Pressure (atm)	$B$ of electron density	$B$ of electron temperature
0.2	-1.206	-0.645 ( $\leq 2 \mu\text{s}$ ), -0.372 ( $\geq 2.5 \mu\text{s}$ )
0.4	-1.336	-0.499
0.6	-1.502	-0.571
1.0	-1.523	-0.603
2.0	-1.669	-0.926

that more absorbers exist at higher pressures. The decaying rate of  $n_e$  is directly related to the recombination reactions.<sup>17</sup> At higher pressure, the recombination reactions are enhanced by higher number density of the particles, and this mechanism would have a great influence on the decaying process.

For electron temperature, the results show that the electron temperature decays faster at higher pressures. However, the fitted results would differ during different periods. At 0.2 atm,  $T_e$  decays proportionally to  $\Delta t^{-0.645}$  before  $2 \mu\text{s}$  and  $\Delta t^{-0.372}$  after  $2.5 \mu\text{s}$ , respectively. This kind of two-stage decay can also be found in other gases (presented in Fig. 9). During the first stage, radiation and expansion are the two dominant quenching channels.<sup>35</sup> The efficiency of these channels decreases rapidly with time as the recombination processes begin to dominate the decay by slightly heating the plasma with the reaction heat, making the value of  $B$  increase during the second stage.<sup>17</sup> However, the two-stage decay pattern disappears as the pressure increases to above 0.4 atm due to the reduction of the measurable time range and the fast quenching at high pressures. In this pressure range, it is hard to find the transition point between the two stages, and one curve can fit all the data.

Figure 9 compares the temporal evolutions of the electron density and temperature of LIP in atmospheric SF<sub>6</sub> with those in atmospheric air and argon. Based on a similar experimental setup, the difference of decaying processes in air and SF<sub>6</sub> can be easily recognized. At  $2 \mu\text{s}$ , the

electron density of SF<sub>6</sub> is slightly higher than that of air. At  $2.5 \mu\text{s}$ , the density of SF<sub>6</sub> drops to the value nearly equal to the density of air plasma. After that, the density of SF<sub>6</sub> is lower than that of air, and the difference between the two gases becomes more obvious. Therefore, the decaying rate in SF<sub>6</sub> is superior to air plasma and argon plasma.

The initial electron temperature of SF<sub>6</sub> plasma is higher than that of air, and after  $3.5 \mu\text{s}$ , it also shows a faster decay. Another feature of the electron temperature decay in SF<sub>6</sub> is that its decaying is slower than the decaying in electron density (time exponents are -0.906 and -0.603, respectively). In contrast, the difference of the decaying rates between the electron density and temperature is not obvious for air or argon plasma (in Ar, the values of  $B$  are -0.74 and -0.72 in electron density and temperature, respectively), except for the decay during the second stage (in air, the values of  $B$  are -0.906 and -0.345 in electron density and temperature). In the field of switch arcs, the dielectric recovery of SF<sub>6</sub> has been studied. According to the simulation of SF<sub>6</sub> arc plasmas (direct current: 50 A) in a nozzle space at atmospheric pressure,<sup>36</sup> it was found that after  $50 \mu\text{s}$ , the electron density dropped from  $1 \times 10^{23} \text{ m}^{-3}$  to  $6 \times 10^{19} \text{ m}^{-3}$ . During the arc decay, both the recombination reactions and the attachment reactions could contribute to the fast loss of the electrons in the plasma.<sup>37</sup> Tanaka *et al.*<sup>38</sup> studied switch arcs in carbon dioxide and SF<sub>6</sub> after current zero via experimental and numerical approaches. They also found that the electron density of SF<sub>6</sub> decreases more rapidly than that of carbon dioxide, which is a result of the faster decay of electron density in SF<sub>6</sub>. However, although the complete ionization exists in both the arc plasma and laser-induced plasma, these two kinds of plasmas are quite different with respect to the way of energy dissipation, energy density, the size of plasmas, etc. Therefore, more work including the numerical modeling should be done to understand the dominant reactions and their effects on decays of electron density and temperature.

#### IV. CONCLUSIONS

In this work, the dynamics of the laser-induced plasmas in SF<sub>6</sub> were obtained by temporally resolved self-emission images, and the evolution of laser-induced SF<sub>6</sub> plasmas at elevated pressures (from 0.2 atm to 2 atm) was quantitatively measured by Thomson scattering. The size of plasmas decreases, and the asymmetry of the plasma occurs

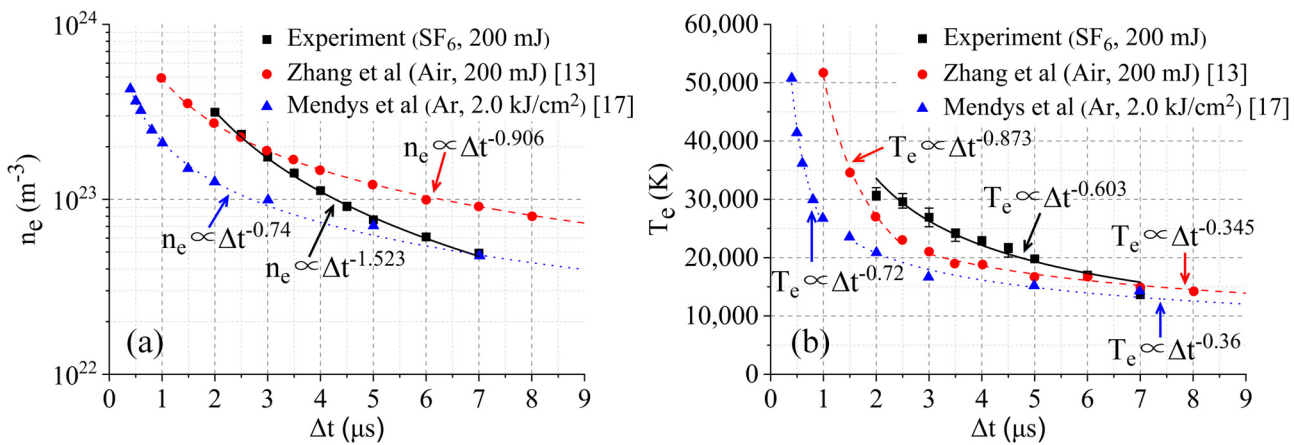


**FIG. 9.** Temporal evolution of the electron density (a) and temperature (b) of LIP in one atmosphere of SF<sub>6</sub>, air, and Ar.

at higher pressures. The time for the transformation into the torus shape decreases at higher pressure. Besides, the appearance of the two-vortex structure indicates the special feature of the dynamics in SF<sub>6</sub> LIP. At 2  $\mu$ s, the electron density around the axis of plasmas increases from  $1.66 \times 10^{23} \text{ m}^{-3}$  to  $3.15 \times 10^{23} \text{ m}^{-3}$  as the pressure increases from 0.2 atm to 1 atm, but this value slightly decreases at 2 atm due to the fast decay at higher pressure. In the meantime, the electron temperature increases from 22 050 K to 44 000 K with increasing pressure. The faster decay at higher pressure is a result of higher recombination rates. The decay of electron density and temperature was fitted using the time exponent of the power law. From 0.2 atm to 2 atm, the exponent for the decay of electron density decreases from -1.206 to -1.669. The exponent for the decay of electron temperature decreases from -0.499 to -0.926 as the pressure increases from 0.4 atm to 2 atm. Two sets of exponents are necessary to describe the decay of electron temperature at 0.2 atm due to the different dominant quenching channels at the two stages. Compared to the laser-induced plasmas in other gases such as air and argon, SF<sub>6</sub> LIP shows superior decay rates of electron density and temperature. More research on the recombination process of SF<sub>6</sub> plasmas will help to explain the difference in the future.

## ACKNOWLEDGMENTS

This work was supported by the National Natural Science Foundation of China under Grant Nos. 51707144 and 51877165 and the State Key Laboratory of Electrical Insulation and Power Equipment (EIPE19302).

## DATA AVAILABILITY

The data that support the findings of this study are available from the corresponding author upon reasonable request.

## REFERENCES

- <sup>1</sup>H. Bluhm, *Pulsed Power Systems, Principles and Applications* (Springer, Berlin, Heidelberg, 2006).
- <sup>2</sup>A. V. Pakhomov and D. A. Gregory, "Ablative laser propulsion: An old concept revisited," *AIAA J.* **38**(4), 725–727 (2000).
- <sup>3</sup>D. W. Hahn and N. Omenetto, "Laser-induced breakdown spectroscopy (LIBS), Part I: Review of basic diagnostics and plasma-particle interactions: Still-challenging issues within the analytical plasma community," *Appl. Spectrosc.* **64**(12), 335A–366A (2010).
- <sup>4</sup>D. R. Welch, D. V. Rose, C. Thoma, R. E. Clark, C. Miller, E. A. Madrid, W. R. Zimmerman, P. K. Rambo, J. Schwarz, and M. Savage, "Kinetic simulation studies of laser-triggering in the Z gas switch," *Phys. Plasmas* **20**(8), 083108 (2013).
- <sup>5</sup>W. R. Rapoport, J. Goldhar, and J. R. Murray, "KrF laser-triggered SF<sub>6</sub> spark gap for low jitter timing," *IEEE T. Plasma Sci.* **8**(3), 167–170 (1980).
- <sup>6</sup>K. J. Nordheden, K. Upadhyaya, Y. S. Lee, S. P. Gogineni, and M. Y. Kao, "GaAs etch rate enhancement with SF<sub>6</sub> addition to BC<sub>3</sub> plasmas," *J. Electrochem. Soc.* **147**(10), 3850 (2000).
- <sup>7</sup>A. Lenk, T. Witke, and G. Granse, "Density and electron temperature of laser induced plasma—a comparison of different investigation methods," *Appl. Surf. Sci.* **96–98**, 195–198 (1996).
- <sup>8</sup>J. Feng, Z. Wang, Z. Li, and W. Ni, "Study to reduce laser-induced breakdown spectroscopy measurement uncertainty using plasma characteristic parameters," *Spectrochim. Acta Part B* **65**(7), 549–556 (2010).
- <sup>9</sup>C. Aragón and J. A. Aguilera, "Characterization of laser induced plasmas by optical emission spectroscopy: A review of experiments and methods," *Spectrochim. Acta Part B* **63**(9), 893–916 (2008).
- <sup>10</sup>S. Zhang, X. Wang, M. He, Y. Jiang, B. Zhang, W. Hang, and B. Huang, "Laser-induced plasma temperature," *Spectrochim. Acta Part B* **97**, 13–33 (2014).
- <sup>11</sup>N. Kawahara, J. L. Beduneau, T. Nakayama, E. Tomita, and Y. Ikeda, "Spatially, temporally, and spectrally resolved measurement of laser-induced plasma in air," *Appl. Phys. B* **86**(4), 605–614 (2007).
- <sup>12</sup>D. Böker and D. Brüggemann, "Temperature measurements in a decaying laser-induced plasma in air at elevated pressures," *Spectrochim. Acta Part B* **66**(1), 28–38 (2011).
- <sup>13</sup>H. Zhang, Y. Wu, H. Sun, F. Yang, M. Rong, and F. Jiang, "Investigations of laser-induced plasma in air by Thomson and Rayleigh scattering," *Spectrochim. Acta Part B* **157**, 6–11 (2019).
- <sup>14</sup>K. Dzierżęga, A. Mendys, S. Pellerin, E. Thouin, G. Travaille, B. Bousquet, L. Canioni, and B. Pokrzywka, "Thomson scattering from laser induced plasma in air," *J. Phys.: Conf. Ser.* **227**, 012029 (2010).
- <sup>15</sup>G. Travaille, A. Mendys, K. Dzierżęga, S. Pellerin, B. Pokrzywka, E. Thouin, B. Bousquet, and L. Canioni, "Study of heating effects during Thomson scattering in laser induced plasma in air," *Contrib. Plasm. Phys.* **51**(2–3), 171–175 (2011).
- <sup>16</sup>E. Nedanovska, D. Riley, T. Morgan, L. Hüwel, and W. Graham, "Thomson scattering and emission spectroscopy of laser sparks induced in pure He and He-N<sub>2</sub> mixtures at 1 atm," *Escampig XXI* (Viana do Castelo, Portuga, 2012).
- <sup>17</sup>A. Mendys, K. Dzierżęga, M. Grabiec, S. Pellerin, B. Pokrzywka, G. Travaille, and B. Bousquet, "Investigations of laser-induced plasma in argon by Thomson scattering," *Spectrochim. Acta Part B* **66**(9–10), 691–697 (2011).
- <sup>18</sup>D. E. Evans and J. Katzenstein, "Laser light scattering in laboratory plasmas," *Rep. Prog. Phys.* **32**(1), 207–271 (1969).
- <sup>19</sup>E. E. Salpeter, "Electron Density Fluctuations in a Plasma," *Phys. Rev.* **120**(5), 1528–1535 (1960).
- <sup>20</sup>K. Warner and G. M. Hieftje, "Thomson Scattering from Analytical Plasmas," *Spectrochim. Acta Part B* **57**(2), 201–241 (2002).
- <sup>21</sup>D. H. Froula, N. C. Luhmann, Jr., J. Sheffield, and S. H. Glenzer, *Plasma Scattering of Electromagnetic Radiation: Theory and Measurement Techniques* (Elsevier, 2011).
- <sup>22</sup>K. Dzierżęga, A. Mendys, and B. Pokrzywka, "What can we learn about laser-induced plasmas from Thomson scattering experiments," *Spectrochim. Acta Part B* **98**, 76–86 (2014).
- <sup>23</sup>E. Nedanovska, G. Nersisyan, T. J. Morgan, L. Hüwel, T. Murakami, C. Lewis, D. Riley, and W. G. Graham, "Investigating the dynamics of laser induced sparks in atmospheric helium using Rayleigh and Thomson scattering," *J. Appl. Phys.* **117**(1), 13302 (2015).
- <sup>24</sup>A. Sasoh, T. Ohtani, and K. Mori, "Pressure effect in a shock-wave-plasma interaction induced by a focused laser pulse," *Phys. Rev. Lett.* **97**(20), 205004 (2006).
- <sup>25</sup>D. Nassif and L. Hüwel, "Appearance of toroidal structure in dissipating laser-generated sparks," *J. Appl. Phys.* **87**(5), 2127–2130 (2000).
- <sup>26</sup>S. Ghosh and K. Mahesh, "Numerical simulation of laser induced breakdown in air," in 46th AIAA Aerospace Sciences Meeting and Exhibit (2008), p. 1069.
- <sup>27</sup>D. Bradley, C. G. W. Sheppard, I. M. Suardjaja, and R. Woolley, "Fundamentals of high-energy spark ignition with lasers," *Combust. Flame* **138**(1–2), 55–77 (2004).
- <sup>28</sup>R. Joarder, G. C. Gebel, and T. Mosbach, "Two-dimensional numerical simulation of a decaying laser spark in air with radiation loss," *Int. J. Heat Mass Transfer* **63**(Aug), 284–300 (2013).
- <sup>29</sup>A. Delseries, F. Y. Khattak, C. L. S. Lewis, and D. Riley, "Optical Thomson scatter from a laser-ablated magnesium plume," *J. Appl. Phys.* **106**(8), 083304 (2009).
- <sup>30</sup>A. Mendys, M. Kański, A. Farah-Sougueh, S. Pellerin, B. Pokrzywka, and K. Dzierżęga, "Investigation of the local thermodynamic equilibrium of laser-induced aluminum plasma by Thomson scattering technique," *Spectrochim. Acta Part B* **96**, 61–68 (2014).
- <sup>31</sup>E. Nedanovska, G. Nersisyan, C. Lewis, and D. Riley, "Investigation of magnesium laser ablated plumes with Thomson scattering," *Laser Part. Beams* **30**(2), 259–266 (2012).
- <sup>32</sup>B. A. Murphy, "Thomson scattering diagnostics of thermal plasmas: Laser heating of electrons and the existence of local thermodynamic equilibrium," *Phys. Rev. E* **69**(1), 16408 (2004).
- <sup>33</sup>B. Pokrzywka, A. Mendys, K. Dzierżęga, M. Grabiec, and S. Pellerin, "Laser light scattering in a laser-induced argon plasma: Investigations of the shock wave," *Spectrochim. Acta Part B* **74**–**75**, 24–30 (2012).

<sup>34</sup>N. Glumac and G. Elliott, "The effect of ambient pressure on laser-induced plasmas in air," *Opt. Laser. Eng.* **45**(1), 27–35 (2007).

<sup>35</sup>G. V. Ostrovskaya, "Laser spark in gases," *Sov. Phys. Usp.* **16**(6), 834 (1974).

<sup>36</sup>K. Murai, T. Nakano, Y. Tanaka, Y. Uesugi, T. Ishijima, T. Shiraishi, T. Shimizu, K. Tomita, K. Suzuki, and T. Fujino, "The LTE simulation on decaying arc plasmas in various arc quenching gases in a model circuit breaker," in 2015 3rd International Conference on Electric Power Equipment-Switching Technology (ICEPE-ST) (2015), p. 146–151.

<sup>37</sup>X. Wang, Q. Gao, Y. Fu, A. Yang, M. Rong, Y. Wu, C. Niu, and A. B. Murphy, "Dominant particles and reactions in a two-temperature chemical kinetic model of a decaying SF<sub>6</sub> arc," *J. Phys. D: Appl. Phys.* **49**(10), 105502 (2016).

<sup>38</sup>Y. Tanaka, T. Nakano, S. Hao, K. Tomita, Y. Inada, A. Kumada, K. Hidaka, T. Fujino, K. Suzuki, and T. Shinkai, "Fundamental studies on switching arcs—Experimental and numerical approaches," in 2017 4th International Conference on Electric Power Equipment-Switching Technology (ICEPE-ST) (2017), pp. 1–10.